ARTICLE   OPEN

Check for updates

Slow and soft passage through tipping point of the Atlantic Meridional Overturning Circulation in a changing climate

Soong-Ki Kim [1], Hyo-Jeong Kim [1], Henk A. Dijkstra[2] and Soon-Il An [1,3] ✉

Paleo-proxy records suggest that the Atlantic Meridional Overturning Circulation (AMOC) exhibits a threshold for an abrupt change, a so-called tipping point. A classical bifurcation theory, a basis of the tipping dynamics of AMOC implicitly assumes that the tipping point is fixed. However, when a system is subjected to time-varying forcing (e.g., AMOC exposed to ice meltwater) an actual tipping point can be overshot due to delayed tipping, referred to as the slow passage effect. Here, using an Earth system model of intermediate complexity and a low-order model with freshwater forcing, we show that the tipping point of AMOC is largely delayed by the slow passage effect. It causes a large tipping lag of up to 1300 years, and strongly relaxes the abruptness of tipping as well. We further demonstrate that the tipping modulation can actively occur in past, present, and future climates by quantifying the effect during Dansgaard-Oeschger events, meltwater pulse 1A (MWP-1A), and current Greenland ice sheet melting. The suggested slow passage effect may explain the observed lagged AMOC collapse to MWP-1A of about 1000 years and provides implications tipping risk in the future.

INTRODUCTION

The Atlantic Meridional Overturning Circulation (AMOC) has a significant impact on the Earth's climate by conveying a large amount of heat northward[1–4]. Its change has a broad climatic impact on the globe, such as on surface temperature, rainfall patterns, and sea ice[5–8]. Paleo-proxy records indicate that meltwater pulses released from ice melt induce variations in the AMOC and resulted in abrupt climate change in the past[2,9–11]. Moreover, the weakened AMOC shown in future climate simulations can significantly modulate the surface warming pattern (e.g., North Atlantic warming hole) response to global warming[6–8].

One of the profound features of AMOC is that it has a certain threshold for abrupt change to occur[12–14]. The prototype model for the AMOC, Stommel's box model[12], offers a classic example. It predicts an abrupt change in the AMOC at a certain level of freshwater forcing by transitioning from a stable state to another, and the threshold is mathematically identified as a bifurcation point. Such thresholds of a system where small perturbation can induce an abrupt and significant change are more generally referred to as a "tipping point". For the AMOC, these are found in a hierarchy of models, including conceptual models[12,15], Earth system models of intermediate complexity[15–17], and even some fully coupled global climate models[18,19]. Especially, the bias-corrected National Center for Atmospheric Research (NCAR) Community Climate System Model (CCSM) showed the rapid collapse of AMOC under doubled atmospheric CO_2 concentration level[19].

The AMOC is exposed to a changing environment (e.g., meltwater pulses from ice), thus, its tipping point should be considered in the context of the response to time-varying external forcing (e.g., freshwater forcing). However, many previous studies rely on the assumption that the AMOC is in a quasi-equilibrium state under transient forcing (i.e., fast adjustment compared to forcing time scale) and do not carefully consider the role of the rate of external forcing[16,20]. Such an approximation may not properly represent the response of the AMOC in a changing climate. From the dynamical system point of view, once the forcing becomes time-dependent, the dynamical system becomes non-autonomous, and new dynamical phenomena appear. When time-varying parameters (e.g., in the forcing) occur, the bifurcation point of the dynamical system can be delayed compared to its bifurcation point under constant parameters, as the state of the system fails to instantaneously adjust to a time-varying parameter. Such an effect is often referred to as bifurcation delay or slow passage effect[21,22] and is ubiquitous in natural phenomena[23–26].

In this study, we investigated AMOC tipping under transient freshwater forcing over a broad range of forcing time scales from decadal to multi-millennial. A series of transient freshwater forcing experiments were performed using Stommel's model and an Earth system model of intermediate complexity, and the impact of the freshwater forcing rate on AMOC tipping was analyzed. We found that the tipping point (i.e., freshwater threshold for an abrupt change), timing, and its abruptness are significantly modulated by transient freshwater flux forcing (FWF), and this variation is denoted as dynamic tipping modulation of the AMOC. Furthermore, we provide examples of the freshwater forcing rates of past, present, and future climate, and demonstrate how tipping modulation operates in a changing climate.

RESULTS

Fundamentals of tipping under stationary freshwater forcing
To obtain basic insights into the tipping process of the AMOC, first, we discuss tipping under stationary freshwater forcing using Stommel's model[12,27], a conceptual AMOC model. In the model, the AMOC is based on salinity and temperature differences between low- and high-latitude ocean boxes (see "Methods"). Modified from the original Stommel's model[12], the temperature

[1]Department of Atmospheric Sciences/Irreversible Climate Change Research Center, Yonsei University, Seoul, Republic of Korea. [2]Institute for Marine and Atmospheric research Utrecht, Department of Physics, Utrecht University, Utrecht, the Netherlands. [3]Division of Environmental Science and Engineering, Pohang University of Science and Technology (POSTECH), Pohang, Republic of Korea. ✉email: sian@yonsei.ac.kr
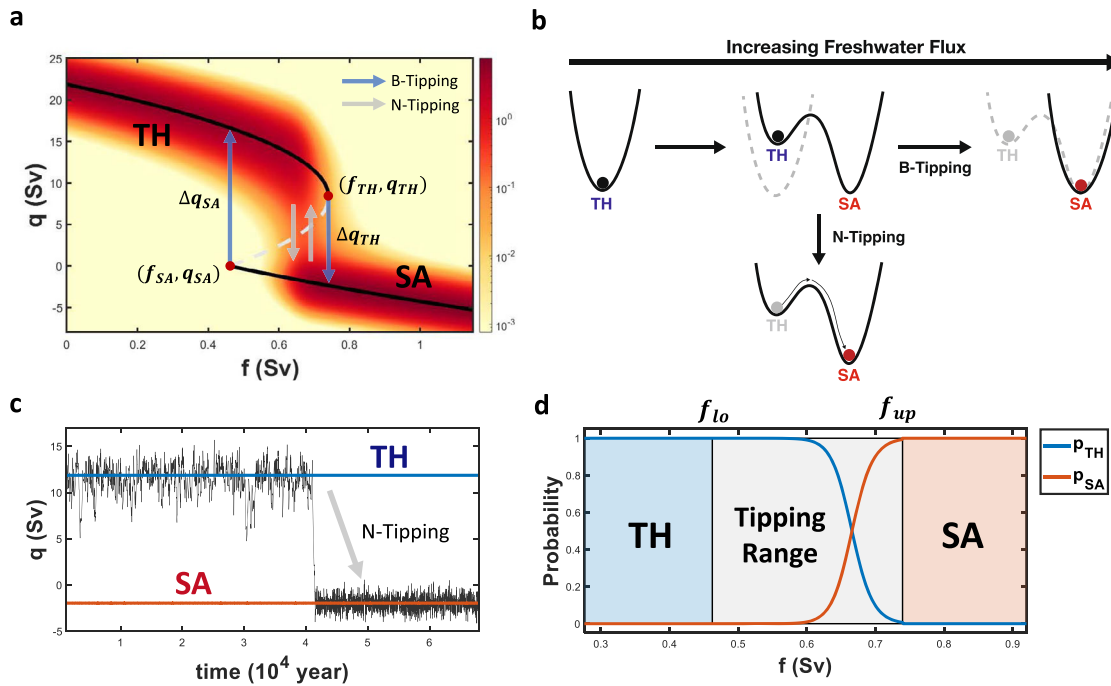
Fig. 1 Tipping behavior in Stommel's model under a stationary freshwater forcing. a Stationary PDF solution of Stommel's model versus the freshwater flux forcing (FWF) represented by f. The color denotes q's normalized PDF, and its local maxima and minima are denoted as black-thick and gray-dashed lines, respectively. The blue and gray arrows schematically illustrate B- and N-tipping processes, respectively. Two bifurcation points, (f_{TH}, q_{TH}) and (f_{SA}, q_{SA}), and their change of q during bifurcation (Δq_{TH} and Δq_{SA}) are marked. **b** Schematic illustration of potential, $V(q)$ in Eq. (8b) with increasing FWF and associated tipping mechanism. **c** Example for N-tipping at $f = 0.73$ Sv. **d** The probability of being in TH (blue line) and SA (orange line) states along FWF. The boundaries of the tipping range (f_{lo} and f_{up}), which are identical to two bifurcation points (f_{TH} and f_{SA}), are marked as a black vertical line.

was fixed, and stochastic forcing was added to the FWF to represent a short time-scale (i.e., weather time-scale) variability[27]. Herein, the FWF in the model is prescribed as a constant value to consider the stationary forcing case. The detailed description and parameters of the model can be found in the Methods section.

The stationary probability density function (PDF) solution of the model is plotted in Fig. 1a (shading), where q and f denote the flow intensity and FWF, respectively. The local maxima (minima) of the PDF, shown by the solid (dashed) line, corresponds to stable (unstable) fixed-point solutions of the model with no FWF noise ($\sigma = 0$) by its mathematical definition. The model exhibits three circulation regimes when varying q: a thermally driven regime with only a polar sinking state (TH; AMOC on), a salinity-driven regime with only an equatorial sinking state (SA; AMOC off), and a multiple-equilibrium regime (with both stable TH and SA states). AMOC tipping occurs through transitions between two stable states (TH and SA), and there are two possible mechanisms for this under stationary forcing: bifurcation (B-tipping) and noise-induced tipping (N-tipping)[28] (Fig. 1b). First, when f passes a bifurcation point, the state evolves to an alternative stable state, resulting in an abrupt change, B-tipping. An AMOC collapse (recovery) by B-tipping, a transition from TH to SA (SA to TH), occurred at $f_{TH} = 0.74$ Sv ($f_{SA} = 0.46$ Sv) with an decrease (increase) of q by $\Delta q_{TH} = 10.9$ Sv ($\Delta q_{SA} = 17.5$ Sv) (1 Sv = 10^6 m³/s) (Fig. 1a). The amplitude of AMOC intensity change for tipping (Δq) was larger for Δq_{SA} than Δq_{TH}, showing asymmetry of collapse and recovery in B-tipping. Here, the Δq quantifies abruptness of tipping for Stommel's model.

Another possible mechanism for tipping is N-tipping. In the bistable regime, the AMOC could transition to another stable state by overcoming the potential barrier with the aid of noise (Fig. 1b, c). To quantitatively assess the N-tipping, the probabilities of being in the TH (p_{TH}) and SA states (p_{SA}) in the bistable regime was determined using the stationary PDF (see "Methods").

The quantities p_{TH} and p_{SA} versus f are plotted in Fig. 1d. As f approached a bifurcation point, the probability of transitioning to the other stable state increased. This is because near the bifurcation point, a low potential barrier provided favorable conditions for a noise-induced transition. An equal-probability point for TH and SA ($p_{TH} = p_{SA} = 0.5$) was located at $f = 0.66$ Sv, which was closer to $f_{TH} = 0.74$ Sv than to $f_{SA} = 0.46$ Sv, showing an asymmetric basin of attraction. For the monostable TH (SA) regime, the probability becomes $p_{TH} = 1$ and $p_{SA} = 0$ ($p_{TH} = 0$ and $p_{SA} = 1$), indicating that N-tipping is not possible in these regimes.

As demonstrated in the N-tipping case, bifurcation points associated with B-tipping (f_{SA} and f_{TH}) did not provide full information on the tipping behavior of the AMOC because noise allowed collapse (recovery) below (above) the bifurcation point level. Instead, these two bifurcation points could be read as lower (f_{lo}) and upper (f_{up}) boundaries of tipping, and we denoted the domain between these boundaries ($f_{lo} \leq f \leq f_{up}$) as the tipping range where $f_{lo} = f_{SA}$ and $f_{up} = f_{TH}$. Later, the tipping range concept was utilized to analyze the tipping under transient freshwater forcing.

Tipping modulation under transient freshwater forcing

The basic features of the AMOC tipping were shown by the stationary forcing case of Stommel's model. However, in more realistic cases, AMOC tipping occurs due to a change in parameters over time. Therefore, f must be considered as a time-varying parameter rather than a fixed value. Herein, we re-investigated AMOC tipping under transient freshwater forcing using Stommel's model, as described in the previous section.

The freshwater forcing parameter f was set as a linearly increasing function with the rate of r passing two bifurcation points (Fig. 2a). The simple linear function can effectively
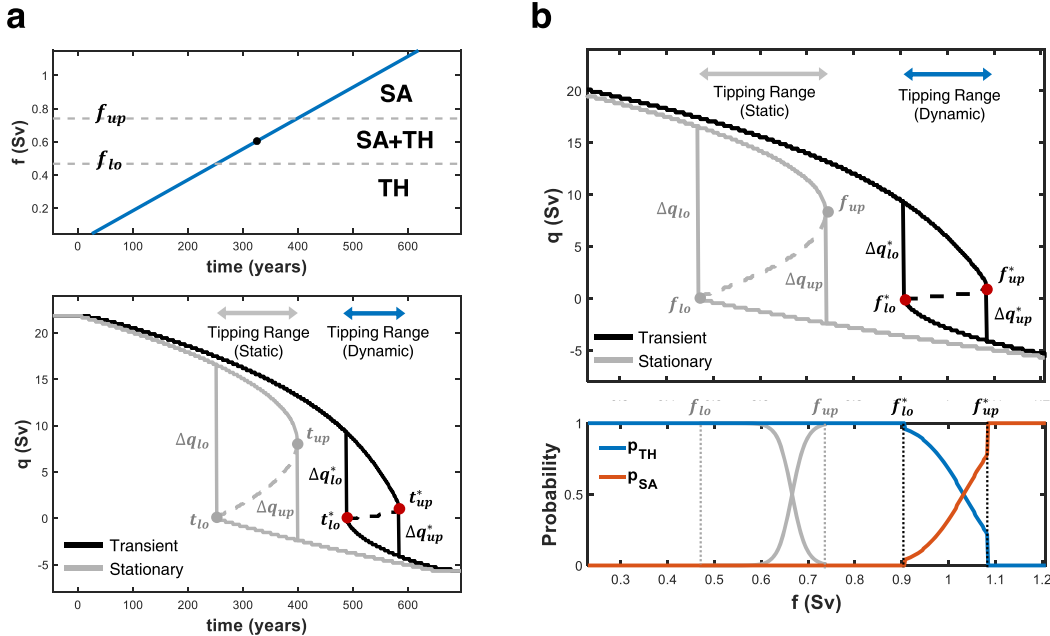
Fig. 2 Demonstration of tipping modulation under transient freshwater forcing using Stommel's model. a In the upper panel, the prescribed freshwater flux forcing (FWF) is plotted. Tipping range boundaries at the stationary FWF (f_{lo} and f_{up}) are marked as a gray-dashed line. In the lower panel, the time evolution of PDF for transient FWF (black line) and stationary FWF (gray line) are plotted. The transient solution was obtained by solving the Fokker–Planck equation (Eq. (7)) with time-varying FWF. The stationary solution was calculated by the stationary PDF (Eqs. (8a) and (8b)) for the FWF value at each time step. The thick and dashed line denoted the local maximum and minimum of PDF, respectively. The time axis is dimensional and time is given in years. **b** In the upper panel, the result in (**a**) is replotted using f as the x-axis. In the lower panel, p_{TH} (blue line) and p_{SA} (orange line) for transient PDF are plotted. The result for stationary PDF was plotted as a gray line for comparison.

characterize the tipping characteristics of AMOC with a rate of the forcing (r). The experiment was set up based on non-dimensional parameters, and the result was demonstrated in dimensionalized quantities (see "Methods"). First, we demonstrated the case for $r = 0.5$ (approximately 1.9 Sv/1000 years $\cong \frac{1}{540}$ Sv/year). The time evolution of q's PDF was calculated with the given linearly increasing FWF by solving the Fokker–Planck equation of Stommel's model (see "Methods"). The Fokker–Planck equation directly retrieved the time evolution of the PDF of the stochastic Stommel model. To compare with Stommel's model solution for a fixed f, the stationary PDF was also calculated for the FWF value f at each time step.

Compared to the stationary response, the tipping behavior of the AMOC was significantly modulated under a transient FWF (Fig. 2). First, the tipping range was delayed, requiring more FWF and time for the AMOC to collapse (i.e., a transiton from TH to SA state). The stationary tipping range (0.46 Sv $\leq f \leq$ 0.74 Sv) shifted to a dynamic tipping range (0.90 Sv $\leq f \leq$ 1.08 Sv), and the half-half probability point increased from 0.66 Sv to 1.04 Sv (see lower panel of Fig. 2b). The delayed tipping range resulted in a delay in timing as well. The static tipping timing range (252 year $\leq t \leq$ 398 year) shifted to a dynamic tipping timing range (488 year $\leq t \leq$ 582 year), and the half-half probability point was delayed for 170 years. Second, the abruptness of the tipping was weakened, and the distance between two stable fixed points over the dynamic tipping range decreased overall. For example, the difference of q between two fixed points at the tipping boundaries (i.e., at the bifurcation points; Δq_{lo} and Δq_{up}) decreased from 17.4 Sv to 10.9 Sv (Δq_{lo} to Δq_{lo}^*) and 17.4 Sv to 4.3 Sv (Δq_{up} to Δq_{up}^*) by 6.6 Sv and 6.6 Sv for f_{lo} and f_{up}, respectively. Because of these decreased Δq_{lo}^* and Δq_{up}^* values, the tipping became less abrupt than that under stationary FWF. However, it should be noted that q values at the tipping boundaries (q_{lo}^* and q_{up}^*) increased, whereas the final q ($q_{lo}^* + \Delta q_{lo}^*$ and $q_{up}^* + \Delta q_{up}^*$) did not change significantly. This indicated

that the underlying mechanism of q changes was not solely by tipping anymore, but rather by a continuous change smoothly following the stable attractor. Third, the tipping range was narrowed. The lower boundary of the tipping range was more delayed than that of the upper boundary, which resulted in the narrowing of the dynamic tipping range under a transient FWF. The width of the tipping range ($f_{up}^* - f_{lo}^*$) decreased from 0.28 Sv to 0.18 Sv, and the corresponding time range width ($t_{up}^* - t_{lo}^*$) decreased from 170 years to 113 years as well.

Next, we performed a sensitivity experiment with varying the FWF rate (r) from $10^{-2.5}$ (approximately 1.2×10^{-5} Sv/year $\cong \frac{1}{85,000}$ Sv/year) to 10^1 (approximately 3.7×10^{-2} Sv/year $\cong \frac{1}{25}$ Sv/year). The value of r was varied by increasing its power δ where $r = 10^\delta$ from -2.5 to 1 with a 3/500 interval. The tipping modulation shown in the previous single-rate experiment ($r = 0.5$) was found for a broad range of r (Fig. 3a–c). The tipping point range was monotonically delayed, and its width decreased as r increased (Fig. 3a). The boundaries of the tipping range increased by up to 2.41 Sv and 2.42 Sv at the fastest case ($r = 3.7 \times 10^{-2}$ Sv/year) for f_{lo} and f_{up}, respectively, showing an almost zero tipping range width. Because the p_{SA} was comparably high near the f_{up}^*, it offered a guiding line that showed a response of tipping characteristics to r. The tipping timing range was also delayed, followed by the delayed point range, but had a non-monotonic relationship with r (Fig. 3b). In the slow regime of r (1.2×10^{-5} Sv/year $< r < 3.7 \times 10^{-5}$ Sv/year), the time to pass through f_{up}^* was further delayed (the delay was maximized at ~1300 years at $r = 3.7 \times 10^{-5}$ Sv/year) as r increased, whereas in the fast regime of r ($r > 3.7 \times 10^{-5}$ Sv/year), the tendency was reversed. There were two competing effects that produce different responses over the slow and fast regimes: (1) an increasing rate of the parameter to approach the tipping point and (2) an increased tipping point value as r increased. On the slow (fast) r, the tipping point delay effect was more (less) dominant than the velocity effect, increasing r, thus, resulting in more (less) delay in the timing. The abruptness of the

a

Collapse

b

Collapse

c

Collapse

d

## Recovery

e

Recovery

f

Recovery
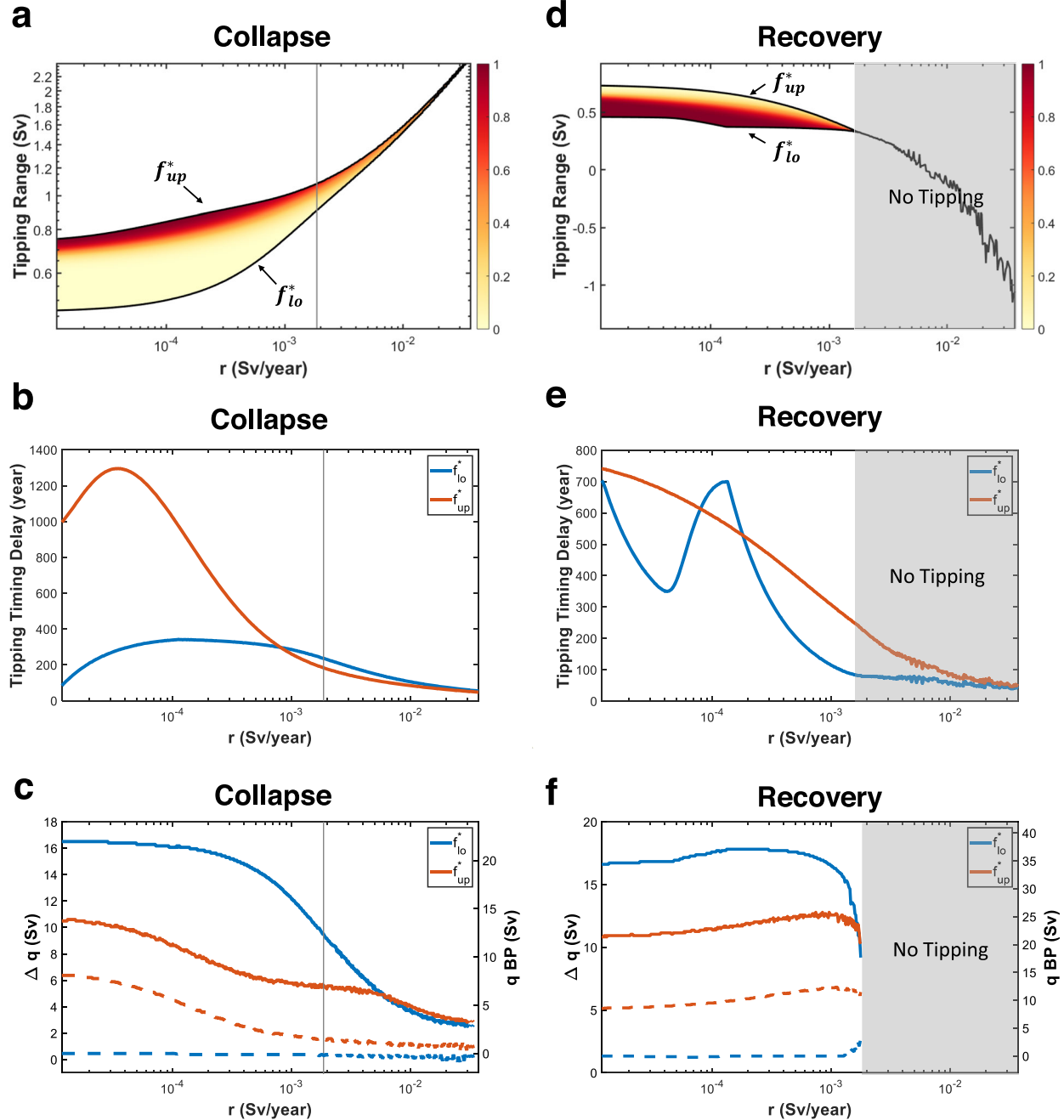
Fig. 3 The tipping modulation experiment with varying freshwater forcing rate using Stommel's model. a A tipping range is plotted with its boundaries, f^*_{lo} (lower black line) and f^*_{up} (upper black line). The red color denotes p_{SA}, the probability for being in the tipped state. **b** A tipping timing delay for f^*_{lo} (blue line) and f^*_{up} (orange line). The time unit is years. **c** The left axis denotes difference of y at the tipping range boundaries, Δy^*_{lo} (blue thick line) and Δy^*_{up} (orange thick line). The right axis denotes y values at the tipping range boundaries, y^*_{lo} (blue dashed line) and y^*_{up} (orange dashed line). On the collapse case, **a**, **b** and **c**, the thin gray line is shown at r = 0.5 (approximately 1.9×10^{-3} Sv/year). The cases shown in Fig. 2d, e, and f are the same as those shown in **a**, **b**, and **c**, respectively, but for the recovery case.

tipping weakened as r increased. The differences in q at the tipping boundaries, Δq^*_{lo} and Δq^*_{up}, were monotonically decreased as r increased (Fig. 3c). They decreased from 17.5 Sv and 10.9 Sv to 2.1 Sv and 2.1 Sv (Δq^*_{lo} and Δq^*_{up}) at the fastest case ($r = 3.7 \times 10^{-2}$ Sv/year) for f^*_{lo} and f^*_{up}, respectively.

Following the collapse case, the recovery tipping was also examined by prescribing decreasing FWF with the same rate but in the opposite direction (see "Methods"). In the recovery, the tipping modulation was also found, but with a much smaller magnitude compared to the collapse. The leading tipping point, f^*_{up} decreased to 0.4 Sv at $r = 1.8 \times 10^{-3}$ Sv/year and the timing delay was maximized with ~750 years at the slowest forcing ($r = 1.2 \times 10^{-5}$ Sv/year). The abruptness of tipping, Δq^*_{up}, decreased to 8.7 Sv, which was comparably less than the collapse. One of the remarkable features was that tipping did not occur anymore over the fast r regime ($r > 1.8 \times 10^{-3}$ Sv/year). The upper and lower tipping boundaries (f^*_{lo} and f^*_{up}) merged into a single point at $r = 1.8 \times 10^{-3}$ Sv/year, indicating that the bistable structure collapsed because of the fast-varying FWF. Over this regime,
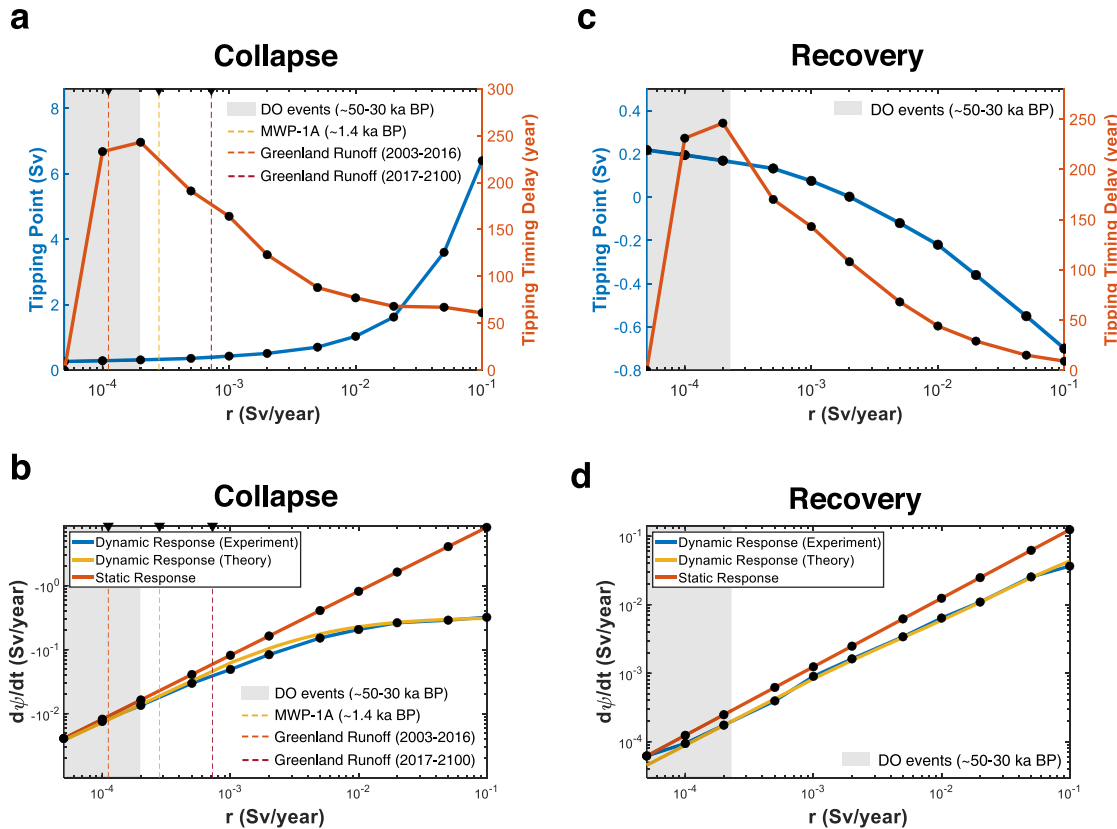
Fig. 4 **The tipping modulation experiment with varying freshwater forcing rate using LOVECLIM. a** The tipping point (left blue side) and the delayed tipping timing (right orange side) compared to the static tipping point along **r** for collapse. **b** The average change rate of AMOC intensity during the collapse. The LOVECLIM experiment result (thick blue line), estimated stationary response (thick orange line), and reproduced changing rate based on the analytical formulation using Eq. (13) (thick yellow line). **c** and **d** are the same as **a** and **b**, respectively, but for the recovery. For **d**, the analytical formulation for recovery (Eq. (14)) was adopted instead of collapse (Eq. (13)). For all subpanels, examples of estimated freshwater flux forcing (FWF) rates are marked (Table 1). Four examples, DO events (gray shading), MWP-1A (dashed yellow line), Greenland ice sheet runoff for 2003–2016 from the GRACE dataset (dashed orange line), and 2017–2100 from the CMIP6 SSP5-8.5 scenario output (dashed red line) are plotted.

the recovery of the AMOC was achieved by a continuous change in q, not by the tipping process, as the stationary solution suggested.

In addition, to examine the robustness of the tipping modulation, we performed the same rate sensitivity experiment for AMOC collapse and recovery, but with (1) different FWF noise amplitudes (original $\sigma = 0.2$ changed to 0.1 and 0.4), and (2) different FWF scenario such as a hyperbolic tangent function (the linear function changed to FWF $\sim$ tanh(rt)). For both experiments, the tipping delay still occurs under different noise amplitudes (Supplementary Fig. 1) and forcing scenarios (Supplementary Fig. 2), but with different magnitudes. The details of these additional experiments can be found in the figure captions of the Supplementary information. The results imply that the tipping delay can robustly occur under various forcing environments, as an intrinsic characteristic of the system.
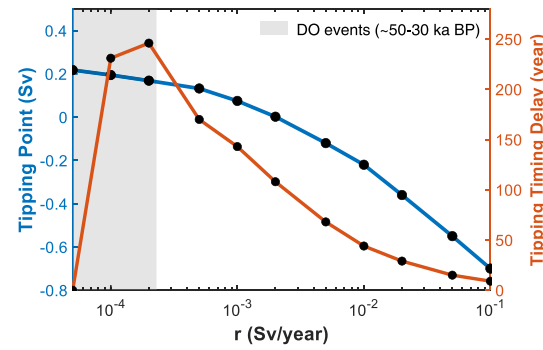
Tipping dynamics in an Earth system model
The results from Stommel's model provided fundamental insights into the dynamic tipping modulation behavior of the AMOC. However, the simplified two-box approximation of the model could not account for all relevant physical processes involved in AMOC behavior. To examine the robustness of the dynamic tipping modulation, we performed an FWF hosing experiment using LOVECLIM. The FWF was prescribed over the North Atlantic region (50°–70°N, 70°–15°W) as a linearly increasing and decreasing function (i.e., AMOC collapse and recovery experiment, respectively). A series of experiments were performed with
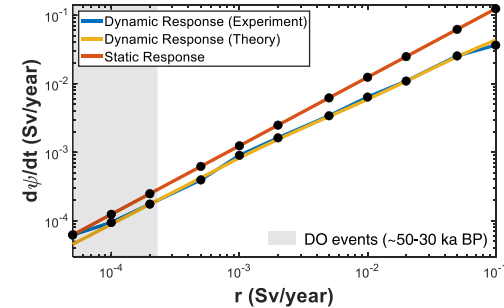
varying FWF rates of 0.1, 0.05, 0.02, 0.01, 0.005, 0.002, 0.001, 0.0005, 0.0002, 0.0001, and 0.00005 Sv/year, which corresponded to 10, 20, 50, 100, 200, 500, 1000, 2000, 5000, 10,000, and 20,000 years to reach 1-Sv forcing. In the LOVECLIM simulation, the exact tipping points could not be calculated analytically. Thus, we measured tipping points as the FWF level where the AMOC intensity crossed its on- and off- states, which was defined as AMOC index level of 2.2 Sv. The detailed experimental configuration and data processing method is described in the "Methods" section. Note that in the LOVECLIM experiment, the tipping point was determined as a single deterministic point, whereas the tipping point was considered in a probabilistic manner (e.g., tipping region) in the previous Stommel's model case.

A significant tipping delay was found in the LOVECLIM model (Fig. 4), similar to Stommel's model. Both the collapse and recovery tipping points were delayed as r increased and had a similar magnitude. The collapse point was linearly increased with r from 0.26 Sv at the slowest case ($r = 5 \times 10^{-5}$ Sv/year) to 6.4 Sv at the fastest case ($r = 10^{-1}$ Sv/year) (Fig. 4a), whereas the recovery point non-linearly decreased from 0.21 Sv at the slowest case to -0.7 Sv at the fastest case, which was considerably less than the collapse (Fig. 4d). The linear sensitivity of collapse tipping point to r was about 12 times larger than the recovery point's, indicating the dynamic tipping modulation is much more active during the collapse than the recovery (see Methods for the details of the estimation).

Following the delayed tipping point, its timing was also delayed with a different response over the slow and fast forcing regimes.

In Figs. 4a and 4c, collapse and recovery shared the same delay feature, including their maxima. In the slow FWF regime (5×10^{-5} Sv/year $\leq r \leq 2 \times 10^{-4}$ Sv/year), collapse and recovery times were more delayed as r increased, whereas in the fast FWF regime ($r \geq 2 \times 10^{-4}$ Sv/year), their timing was less delayed (Fig. 4b). Their delays were maximized at $r = 2 \times 10^{-4}$ Sv/year for ~250 years. The different timing delays over the slow and fast forcing regimes could be explained by the two competing effects discussed in Stommel's model case. Comparing the amount of delayed timing for collapse and recovery, they showed a large difference in the fast FWF regime, in contrast to having almost the same delay in the slow forcing regime. At the fastest forcing ($r = 10^{-1}$ Sv/year), the collapse was delayed by ~60 years, whereas the recovery was delayed by ~10 years.

The abruptness of tipping can be measured by the rate of the AMOC intensity change. It is written in a decomposed form as follows:

$$\frac{d\psi}{dt} = \frac{d\psi}{df} \times \frac{df}{dt}. \tag{1}$$

where ψ denotes AMOC intensity (note that the definition of abruptness is slightly different from the Stommel's model case). The change in the AMOC intensity with FWF was approximated as $\frac{d\psi}{df} \approx \frac{\Delta\psi}{\Delta f}$. The dynamic tipping modulation was read as a change in $\frac{\Delta\psi}{\Delta f}$. Under the stationary forcing picture, $\frac{\Delta\psi}{\Delta f}$ was assumed to be constant. In contrast, under transient forcing, $\frac{\Delta\psi}{\Delta f}$ depended on the forcing rate (Figs. 2–4). That is, dynamic tipping modulation could affect the rate of change of the AMOC strength. Because of the delayed tipping point, the AMOC required more FWF to reach the same strength (i.e., increased Δf with fixed $\Delta\psi$), which resulted in a decrease in the rate of AMOC change. Here, we denote the decelerated change in the AMOC owing to the transient FWF as a dynamic deceleration effect.

The LOVECLIM results were analyzed to quantitatively assess the dynamic deceleration effect. The average AMOC intensity change rate during the collapse and recovery was calculated from the time series output (see Supplementary Fig. 3 for details). To demonstrate the dynamic deceleration effect, the stationary response (i.e., $\frac{d\psi}{dt}$ with constant $\frac{d\psi}{df}$) was estimated using Eq. (1) by replacing $\frac{d\psi}{df}$ with the slowest experimental value ($r = 5 \times 10^{-5}$ Sv/year). The results are plotted in Fig. 4b and d for the collapse and recovery, respectively. The simulated collapse rate of the AMOC (blue line) was significantly reduced compared to the static response (orange line), and the difference increased as r increased. While the stationary response predicted a linear increase in the AMOC rate with r, the LOVECLIM results showed a nonlinear increase with r having saturated characteristics. At the fastest FWF ($r = 10^{-1}$ Sv/year), the static response predicted -8.17 Sv/year of collapse rate whereas the LOVECLIM results gave -0.32 Sv/year, showing a 97% decrease of the changing rate. The recovery rate of the AMOC was also lower than that of the stationary response, but the amount was much less than that of the collapse. At the fastest FWF ($r = 10^{-1}$ Sv/year), the stationary response predicted 0.12 Sv/year whereas the LOVECLIM results gave 0.03 Sv/year, showing a 75% decrease.

The dynamic deceleration effect is essentially caused by the tipping delay effect. To quantitatively understand the link between them, we mathematically formulated the dynamic deceleration effect explicitly linking it with the tipping delay effect. A delayed tipping point under the transient FWF can be written as follows:

$$f_{dyn}(r) = f_{st} + f_{delay}(r). \tag{2}$$

Under linear forcing with a rate of r, the static tipping point (f_{st}) is delayed to the dynamic tipping point (f_{dyn}) due to tipping modulation by the transient FWF, with a delay of f_{delay}. Assuming

the AMOC was in an initial state with FWF level f_0 and tipping had occurred at f_{dyn} with AMOC intensity change of $\Delta\psi$, then the abruptness of the tipping is written as follows by substituting Eq. (2) into Eq. (1):

$$\frac{d\psi}{dt} \approx \frac{\Delta\psi}{\Delta f} \times r = \frac{\Delta\psi}{f_{st} - f_0 + f_{delay}(r)} \times r. \tag{3}$$

The formulation clearly illustrates that the delay of tipping point (f_{delay}) decreases the abruptness of tipping ($\frac{d\psi}{dt}$). The notable thing is that the tipping delay effect (f_{delay}) holds the upper limit level of the abruptness of tipping. The maximum abruptness of tipping at fast FWF limit ($r \to \infty$) is written as follows by applying the L'Hôpital's rule on the Eq. (3):

$$\lim_{r \to \infty} \frac{d\psi}{dt} = \Delta\psi \times \lim_{r \to \infty} \frac{r}{f_{st} - f_0 + f_{delay}(r)} = \Delta\psi \times \left(\lim_{r \to \infty} \frac{df_{delay}}{dr} \right)^{-1}. \tag{4}$$

For the simplest example, assuming that the tipping point is linearly delayed to r, $f_{delay} = k \times r$ (approximately reasonable as shown in Fig. 4a and b), the tipping abruptness at the fast FWF limit becomes $\Delta\psi/k$. If there is no tipping delay effect ($f_{delay} = 0$), the abruptness linearly intensifies without upper limit as r increases (see Eq. (3)). It shows that the tipping delay effect can limit the maximum level of changing rate of AMOC, as a brake to the system.

The maximum level for AMOC collapse and recovery is estimated based on the LOVECLIM experiment results. First, the tipping point delay curve is fitted, then the tipping abruptness ($\frac{d\psi}{dt}$) is reproduced based on the fitted tipping point (see Methods for details). The reproduced collapse rate captured the overall behavior with a good agreement with a negligible difference, indicating that the formulation was reliable (see yellow line in Fig. 4a and c). The estimated tipping abruptness at a fast FWF limit ($r \to \infty$) is 0.32 Sv/year for collapse, and 3.96 Sv/year for the recovery, about 12 times larger for the recovery than collapse. Since the tipping point delay is much more active for the collapse than the recovery, the following dynamic declaration effect is more intense during the collapse, largely suppressing/limiting the change rate of AMOC.

Dynamic tipping modulation in a past, present, and future climate

The series of transient FWF experiments showed the general tipping characteristics of the AMOC under a broad range of FWF rates. To understand such tipping dynamics in a practical context, the typical value of the observed FWF rate should be provided. Here, we introduce examples of freshwater forcing rates that may have had a profound impact on the past as well as on the present and future of Earth's climate.

First, we introduce two major meltwater release examples that occurred in the past, Dansgaard-Oeschger (DO) events that occurred ~30,000–50,000 years ago, and meltwater pulse 1A (MWP-1A), which occurred ~14,000 years ago. DO events are characterized by a series of rapid warming and cooling of the Northern Hemisphere[29], and paleo-proxy records show that a massive amount of freshwater from ice was discharged to the North Atlantic and weakened the AMOC[30,31]. MWP-1A is known as the largest meltwater pulse during the last deglaciation[32] and is inferred to have caused a sea-level rise of ~20 m[33]. The model experiment study suggests that the AMOC weakened during this period by freshwater inflow into the North Atlantic[32]. The FWF rates of these examples were estimated using reconstruction data[34,35] (see Table 1 and "Methods"). Because the reconstructed FWF time series for these events showed oscillatory- and pulse-like shape functions for DO[34] and MWP-1A events[35], respectively, the truncated-linear rates of FWF variation are estimated, reflecting

Table 1. The estimated rates of FWF.

Example	Period	Linear FWF rate (Sv/year)	FWF source	Source data type	Reference
DO events	~50–30 ka BP	-2.3×10^{-4}~1.9×10^{-4}	North Atlantic freshwater imposed by LOVECLIM	Reconstruction (LOVECLIM with SST proxy)	Ref. [34]
MWP-1A	~1.4 ka BP	2.8×10^{-4}	North America ice sheet	Reconstruction (Glimmer-CISM with Ice-5G)	Ref. [35]
Greenland runoff	2003–2016	1.1×10^{-4}	Greenland ice sheet	Observation (GRACE)	Ref. [44]
	2017–2100	7.2×10^{-4}	Greenland ice sheet	GCM Projection (CMIP6 SSP5-8.5)	Ref. [45]

overall time scales and FWF levels (see "Methods"). Thus, it can provide a tipping modulation effect in a highly approximated manner.

The linear FWF rates for DO and MWP-1A events are plotted in the LOVECLIM sensitivity experiment results (Fig. 4). The FWF rates of these cases are in the relatively slow FWF regime, characterized by large tipping timing delays and small tipping point delays. The maximum rate of DO events (MWP-1A) induced a tipping point delay from 0.26 to 0.31 Sv (0.33 Sv) and tipping point timing delay for 243 years (234 years). This highlights the counterintuitive tipping timing delay over the FWF rate. As previously mentioned, the competition between the delaying tipping point and FWF rate can produce a large tipping timing delay, even if the tipping point is not significantly delayed. Interestingly, such a timing delay can be found in the proxy record for the MWP-1A case. The proxy records show that the MWP-1A occurred ~1000 years before the associated significant change in AMOC happened[2,36,37]. A previous study argued that such a paradox can be resolved if the MWP-1A originates largely from the Antarctic ice sheet[2]. However, a recent study suggested that MWP-1A mainly originated from North America, and the contribution of Antarctica is relatively small[38]. Therefore, as an alternative, the tipping timing delay effect can explain the delayed response of the AMOC to MWP-1A.

Next, we introduced an FWF rate example that had profound implications for the present and future climate, that is, Greenland ice sheet melting. Observations have showed that meltwater runoff of Greenland has accelerated during recent decades[39,40], and it raises a concern that the AMOC may collapse due to this melting[41–43]. The FWF rate of Greenland runoff was estimated for two different periods, 2003–2016 and 2017–2100, using an observational dataset[44] and Socioeconomic Pathway 5-8.5 (SSP5-8.5) scenario output of regional downscaled Coupled Model Intercomparison Project Phase 6 models[45], respectively (see "Methods").

The FWF rate of Greenland runoff from 2003 to 2016 was similar to that of the DO and MWP-1A events (Fig. 4 and Table 1). At this rate, the tipping point and its timing are delayed by 0.02 Sv and 224 years, respectively. However, the projected runoff rate for 2017–2100 under the SSP5-8.5 scenario was larger than the present day rate from 2003 to 2016 (Fig. 4 and Table 1). At this rate, the tipping point and its timing were delayed by 0.14 Sv and 170 years, respectively, showing a larger (less) tipping point (tipping timing) delay than previous examples. This demonstrated that an increased Greenland meltwater runoff rate could modulate the tipping characteristics of the AMOC, possibly towards a less lagged response to freshwater forcing. Because the regional downscaled CMIP6 output underestimated the runoff rate compared to the observation (see Methods), these modulation effects may be underestimated.

DISCUSSION

Our results showed that the threshold of abrupt collapse and recovery (i.e., tipping point) of the AMOC largely depends on the

changing rate of external forcing exerted. A series of linear FWF experiments using Stommel's model and LOVECLIM suggested that the tipping point, its timing, and abruptness are strongly modulated by transient FWF, denoted as dynamic tipping modulation. As the changing rate of FWF increases, the tipping point is significantly delayed (i.e., increase for collapse and decrease for recovery), and its abruptness is largely weakened (i.e., decrease in the AMOC intensity change rate) by the slow AMOC adjustment to a changing FWF. The tipping timing is also delayed, followed by the delayed tipping point, but it is rather weaker as the rate of FWF increases, and is maximized at a slow FWF rate, even if the tipping point is not delayed significantly. Such a counterintuitive tipping timing delay emerges from the competition between increasing distance to the tipping point and increasing rate to reach the tipping point. Furthermore, dynamic tipping modulation is much stronger on collapse tipping than recovery tipping.

To understand the effect of tipping modulation dynamics, we introduced examples of freshwater forcing rates that have profound implications on the past, present, and future of Earth's climate. Although these examples estimate tipping modulation in a highly approximated manner, they highlight the complexity of tipping delay dynamics over a wide range of FWF rates. An example of DO and MWP-1A events emphasizes the importance of nonlinear tipping timing dynamics, which induces a large tipping timing delay over the slow FWF rate. This may be responsible for about 1,000 years of tipping delay between MWP-1A and the associated AMOC change, as seen in the proxy records. In addition, an example of Greenland runoff demonstrated that the tipping timing delay effect may be weakened owing to an increased FWF rate by accelerated ice sheet melt.

This study facilitates understanding of AMOC changes caused by freshwater forcing. The dynamic tipping modulation effect may be reflected in the results of many studies with freshwater hosing experiments, and our research can help to understand the result in a more refined way. For example, ref. [18] imposed FWF at a rate of $r = 0.0005 \, \text{Sv/year}$ over the North Atlantic region using the FAMOUS atmosphere-ocean coupled global climate model (AOGCM) and compared it with the equilibrium solution under static freshwater forcing. Their results showed that about 0.2 Sv tipping point delay occurred by transient FWF, while our study using LOVECLIM predicted a tipping delay of 0.06 Sv at this FWF rate. This implies that there is an inter-model difference in the tipping modulation effect. The diffusivity in an ocean model can be one of the main factors for inter-model diversity in the tipping modulation effect[17].

Moreover, our study can provide a basis for understanding the tipping modulation effect under various forcing scenarios. The ref. [26] investigated AMOC tipping under CO_2 overshooting scenario (i.e., reversing the forcing to its initial level) using the modified Stommel's model, and showed the tipping can be avoided even if the system is across the tipping threshold. Such returnability of the system can be understood as a result of the tipping delay effect shown in this paper. Even if the system across

the static tipping point, the tipping can be avoided if the forcing is quickly reversed before reaching its dynamic tipping point.

Physically, the tipping delay occurs because the tipping point is likely to be determined by the total amount of freshwater over the AMOC convection region, rather than the FWF level itself[46]. The total amount of freshwater is a key factor that influences surface density and stratification of the deepwater formation region. Therefore, the tipping does not occur until the total accumulated amount of freshwater reaches a certain threshold, even if the FWF level is across the static tipping point. Specifically, it is determined by the time-integrated quantity of FWF and the horizontal distribution of the forcing by oceanic circulation feedback (e.g., freshwater/salt advection), and atmospheric feedback (e.g., hydrological cycle). An in-depth discussion of physical mechanisms is out of the scope of this paper, focusing on the tipping modulation phenomenon itself. In addition, the asymmetry of collapse and recovery tipping point delay would be related to the nonlinear salt-advection feedback of AMOC, positive feedback that reinforces/weaken the circulation to FWF[17,47]. On the AMOC on state, the circulation is actively influenced by the positive nonlinear salt-advection feedback, thus the freshwater forcing can largely weaken AMOC (i.e., sensitive response to FWF). In contrast, on the AMOC off state, the salt-advection feedback is weak, thus the freshwater forcing cannot largely strengthen AMOC (i.e., insensitive response to FWF). Therefore, tipping delay more largely occurs during the collapse (i.e., AMOC on to off state) than the recovery (i.e., AMOC off to on state).

In addition, it should be noted that there is another possible tipping mechanism when the system is exposed to time-varying external forcing, so-called rate-induced tipping[28] (R-tipping). If the rate of the forcing is sufficiently fast, some types of the system exhibit advancement of tipping point, which is the exact opposite case of delayed tipping. It is an essentially different tipping mechanism discussed in this paper. The tipping delay effect is related to the inertia of the system, whereas the R-tipping is caused by failure of adjusting to the equilibrium state due to fast-varying forcing (i.e., the inertia effect doesn't work anymore). Some of the previous studies demonstrated that the R-tipping can possibly occur for AMOC collapse in certain types of models, such as in a low-order model[48] and a global ocean model[49]. However, in our series of experiments, we couldn't find R-tipping, but only for the delay effect even if the unrealistically large rate of FWF was exerted (Figs. 3 and 4). Such difference between previous studies might be caused by inter-model differences in AMOC simulation[16] or our experiment's forcing was not fast enough to induce the R-tipping. It remains unknown whether the R-tipping is possible for AMOC.

METHODS

Stommel's model

In Stommel's model, the AMOC is based on salinity and temperature differences between low- and high-latitude ocean boxes[12]. The temperature of each box had a fixed value, and a stochastic forcing was added to the FWF to represent short time-scale (i.e., weather time-scale) variability[27]. The non-dimensional salinity difference between the two boxes (y) satisfied the following dimensionless equation:

$$\frac{dy}{dt} = -(1 + \mu|y - 1|)y + f(t) + \sigma\xi(t) \tag{5}$$

Here, $f(t)$ denotes the FWF and μ represents the ratio of diffusive and advective time-scales. $\xi(t)$ is Gaussian white noise with zero mean and unit variance and σ denotes the amplitude of the noise. The strength of flow (q) could be parameterized as the exchange rate between the two boxes, as follows:

$$q = c(a_x x - a_y y) \tag{6}$$

where x is the fixed temperature difference between the two boxes, c is a tunable parameter, and a_x and a_y are the thermal and haline expansion coefficients, respectively.

To directly retrieve the PDF of q, Eq. (5) was transformed into the Fokker–Planck equation as follows:

$$\frac{\partial p}{\partial t} = -\frac{\partial}{\partial y}\left[-(1 + \mu|y - 1|)yp + f(t)p\right] + \frac{1}{2}\sigma^2\frac{\partial^2 p}{\partial^2 y} \tag{7}$$

where p is the probability density of y. The Fokker–Planck equation was solved with central differences and the implicit Euler time integration method. The numerical parameters were set as $\Delta t = 0.01$ and $\Delta y = 0.01$ within the $y = [-0.5, 2.5]$ domain. The initial condition was set as a Dirac delta function centered at $y = 0.5$ as follows: $p(y) = \delta(y - 0.5)$, and 200 years spin-up time was given for an adjustment to an initial f. Parameters were fixed as $\mu = 4.2$ and $\sigma = 0.2$. The obtained PDF of the y ($p = p(y)$) was converted to the PDF of q ($p = p(q)$) using Eq. (6).

The dimensionless quantities in Eq. (7) were converted into dimensional values according to ref. [27] by $y' = y_d y$, $f' = f_d f$, and $t' = t_d t$, where $y_d = 5.67$ psu, $f_d = 0.46$ Sv, and $t_d = 124$ years, where the superscript ′ denotes dimensional quantity. The dimensional exchange rate (q') was obtained from y' and dimensional parameters $a_x = 1.7 \times 10^{-4}\,^\circ\text{C}^{-1}$, $a_y = 7.5 \times 10^{-4}$ psu^{-1}, $x = 25\,^\circ$C, and $c = 5145$ Sv.

Stationary PDF solution of Stommel's model

For the stationary FWF, the analytical PDF solution of Stommel's model was obtained by solving the Fokker–Planck equation (Eq. (7)) with $\frac{\partial p}{\partial t} = 0$. Here, $f(t)$ was a constant. The stationary PDF solution (p_{st}) for y was expressed as follows:

$$p_{st} = N\exp\left(-\frac{2V(y)}{\sigma^2}\right) \tag{8a}$$

where

$$V(y) = \begin{cases} \frac{1}{2}(1 + \mu)y^2 - \frac{1}{3}\mu y^3 - fy, 0 < y < 1 \\ \frac{1}{2}(1 - \mu)y^2 + \frac{1}{3}\mu y^3 - fy + \frac{1}{3}\mu, 1 < y \end{cases} \tag{8b}$$

In these equations, $V(y)$ denotes the potential of the system and N denotes a normalization coefficient. The system prefers low potential energy, which corresponds to a high PDF value. The local maxima (minima) of the PDF corresponded to the stable (unstable) fixed-point solutions of Eq. (5) with no noise ($\sigma = 0$) by its mathematical definition ($\frac{\partial V}{\partial y} = \frac{\partial y}{\partial t} = 0$). In the main text, the obtained PDF of the y ($p = p(y)$) was converted to the PDF of q ($p = p(q)$) using Eq. (6).

Calculation of p_{TH} and p_{SA}

The probability of being in the TH (p_{TH}) and in the SA state (p_{SA}) in the bistable regime was determined using the PDF solution of Stommels' model ($p(y)$) as follows:

$$p_{TH} = \int_{-\infty}^{y_{min}} p(y)dy, \tag{9a}$$

$$p_{SA} = \int_{y_{min}}^{\infty} p(y)dy, \tag{9b}$$

where y_{min} is the local minimum of the PDF.

Stommel's model experiment

In the transient FWF experiment using Stommel's model, the FWF was set as a linearly increasing function with a rate of r passing two bifurcation points as follows:

$$f(t) = a + r(t - t_c) \tag{10}$$

where $a = 1.13$ (~0.5 Sv) and $t_c = 800$ (~98,400 years) (upper panel of Fig. 2a). Here, t_c only affected the model time year and did not fundamentally change the solution. We carried out a series of experiments with varying r. The Fokker–Planck equation of Stommel's model (Eq. (7)) was solved using the given time-varying FWF (Eq. (10)), and the time evolution of y's PDF was calculated. The recovery experiment was performed by replacing r with $-r$ in Eq. (10), starting from the endpoint of the collapse case. In the main text, we re-zeroed the model time by transforming the time coordinate as follows, $t' = t - 797.37$.

LOVECLIM experiment configuration and analysis

We utilized the ECBilt-CLIO-VECODE-LOCH-AGISM (LOVECLIM), which is a three-dimensional Earth system model of intermediate complexity[50].

The atmospheric model[51] (ECBilt) solved the potential vorticity equation using a spectral method at a horizontal resolution of ~5.6°. The oceanic component[52] (CLIO) was a general circulation model with a horizontal resolution of 3° and a vertical resolution of 20 levels. The vegetation model VECODE[53] utilizes plant functional type classification. The ice sheet and carbon cycle models were not activated in this study.

For the hosing experiment, we applied linearly increasing and decreasing FWF at different rates (from 5×10^{-5} to 10^{-1} Sv/year), which is uniformly distributed in the North Atlantic region (50°–70°N, 70°–15°W). In the AMOC collapse experiments, the forcing was held constant once it reached a predefined maximum value. For relatively slow forcing cases ($r < 10^{-2}$ Sv/year), the maximum was set to 1 Sv. For the faster-forcing cases ($r \geq 10^{-2}$ Sv/year), the AMOC did not collapse until the forcing met 1 Sv (i.e., the tipping point was beyond 1 Sv), so the maximum value was adjusted to 10 Sv. The AMOC recovery experiments were performed in the same way, but with opposite signs in the forcing. The AMOC intensity was measured by the maximum overturning stream function in the North Atlantic (>20°N), below 500 m. A low-pass filter with a cutoff period of 20 years was applied to the raw AMOC intensity time series to eliminate high-frequency variability. The time series of filtered AMOC intensity for the LOVECLIM experiments is presented in Supplementary Fig. 3. The collapse and recovery tipping point was measured as FWF level where the filtered AMOC intensity (ψ) crossed 2.2 Sv following ref. [46] (see Supplementary Fig. 3).

Fitting LOVECLIM experiment results

The tipping points for LOVECLIM experiment results (Fig. 4a and c) were fitted. The collapse tipping point was fitted as:

$$f_{\text{collapse}} = f_{st} + k_{\text{collpase}} \times r \qquad (11)$$

where $f_{st} = 0.26$ Sv and $k_{\text{collapse}} = 62.78$ years ($R^2 = 0.99$), and the recovery tipping point was fitted as:

$$f_{\text{recovery}} = f_1 + k_{\text{recovery}} \times r + (f_{st} - f_1) \times e^{-ar} \qquad (12)$$

where $f_1 = -0.2247$ Sv, $k_{\text{recovery}} = -5.105$ year, and $a = 374.4$ year/Sv ($R^2 = 0.98$). The k_{collapse} and k_{recovery} characterize linear sensitivity of the dynamical tipping point to r for collapse and recovery, respectively.

Based on the fitted curve (Eqs. (11) and (12)), the abruptness of the tipping was reproduced. Substituting Eq. (11) to Eq. (3), the abruptness of collapse tipping was written as follows:

$$\frac{d\psi}{dt} \approx \frac{\Delta\psi}{f_{st} - f_0 + k_{\text{collapse}} \times r} \times r \qquad (13)$$

and for the recovery:

$$\frac{d\psi}{dt} \approx \frac{\Delta\psi}{f_1 - f_0 + k_{\text{recovery}} \times r + (f_{st} - f_1) \times e^{-ar}} \times r. \qquad (14)$$

The abruptness of collapse (recovery) tipping at the fast FWF limit ($r \to \infty$) is $\frac{\Delta\psi}{k_{\text{collapse}}} = 0.32$ Sv/year ($\frac{\Delta\psi}{k_{\text{recovery}}} = 3.96$ Sv/year).

Estimation of the FWF rate

The FWF rate of the DO events was estimated using the FWF reconstruction data from ref. [34]. The authors reconstructed FWF over the North Atlantic (50–65° N, 50–10° W) during DO events (~50–30 ka before present) using LOVECLIM and alkenone-based SST proxy reconstruction. The reconstructed FWF sinusoidally varies between positive and negative values (see Fig. 2 of ref. [34]). The range of FWF rate of DO events was estimated with a difference in fluctuating FWF.

The rate of MWP-1A events was estimated using MWP-1A reconstruction from ref. [35]. They reconstructed the FWF from the North American ice sheet during MWP-1A using the Glimmer-CISM ice sheet model and validated it with Ice-5G ice sheet reconstructions. The reconstructed FWF for MWP-1A followed a pulse-like shape function (see Fig. 2c in ref. [35]). The FWF rate of MWP-1A was estimated by the linear trend between the FWF level at MWP-1A onset (~12.1 kyr ago in model time) and peak (~11.6 kyr ago in model time).

The rate of Greenland runoff from 2003 to 2016 was obtained from the monthly Gravity Recovery and Climate Experiment (GRACE) mass balance dataset[44]. The ice runoff per year (Gt/year) was calculated by the difference in yearly averaged runoff (Gt) and converted into an equivalent amount of FWF (Sv). The increasing linear trend of FWF was calculated for 2003–2016, estimated as the FWF rate (Sv/year).

The projected Greenland runoff rate for 2017–2100 was estimated from the regional downscaled CMIP6 experiment output from ref. [45]. The annual surface mass balance (SMB) of Greenland (Gt/year) for 1950–2100 combined historical (1950–2014) and SSP5-8.5 (2015–2100) scenario runs, and the ensemble mean of five models (CESM2, CNRM-CM6-1, CNRM-ESM2-1, MRI-ESM2-0, and UKESM1-0-LL) was calculated. The annual SMB (Gt/year) was converted into an equivalent amount of FWF (Sv). The linear FWF rate was calculated using the FWF difference between 2017 and 2100. To compare the FWF rate with the GRACE dataset (2003 to 2016), the FWF rate for 2003 to 2016 was also calculated as 5.7×10^{-5} Sv/year. It was smaller than the rate from the GRACE dataset (1.1×10^{-4} Sv/year).

Note that the source regions of FWF in the above examples were different from the LOVECLIM experiment, which imposed FWF forcing over 50°–70°N, 70°–15°W, thus, caution should be taken when interpreting the results (Fig. 4). For example, FWF during DO events is reconstructed based on 50–65° N, 50–10° W (ref. [34]), while the LOVECLIM experiment imposed FWF over 50°–70° N, 70°–15°W. Therefore, these rates do not precisely correspond to the rate imposed on the LOVELCIM experiment. Nevertheless, the FWF sources of these examples are similar to those of our experiment (e.g., DO events in the North Atlantic) and major freshwater contributors in the North Atlantic region[38,54] (e.g., Greenland ice sheet and MWP-1A in the North America ice sheet). They thus provide a typical rate of FWF over the North Atlantic region in a highly approximated manner. In addition, it should be noted that there is an uncertainty of estimated rates for MWP-1A and DO events.

REFERENCES

1. Rahmstorf, S. On the freshwater forcing and transport of the Atlantic thermohaline circulation. *Clim. Dyn.* **12**, 799–811 (1996).
2. Clark, P. U., Pisias, N. G., Stocker, T. F. & Weaver, A. J. The role of the thermohaline circulation in abrupt climate change. *Nature* **415**, 863–869 (2002).
3. Rahmstorf, S. Ocean circulation and climate during the past 120,000 years. *Nature* **419**, 207–214 (2002).
4. Zhang, R. et al. A review of the role of the Atlantic Meridional Overturning Circulation in Atlantic multidecadal variability and associated climate impacts. *Rev. Geophys.* **57**, 316–375 (2019).
5. McManus, J. F., Francois, R., Gherardi, J.-M., Keigwin, L. D. & Brown-Leger, S. Collapse and rapid resumption of Atlantic meridional circualtion linked to deglacial climate changes. *Nature* **428**, 834–837 (2004).
6. Kim, H. & An, S.-I. On the subarctic North Atlantic cooling due to global warming. *Theor. Appl. Climatol.* **114**, 9–19 (2013).
7. Keil, P. et al. Multiple drivers of the North Atlantic warming hole. *Nat. Clim. Chang.* **10**, 667–671 (2020).
8. Liu, W., Fedorov, A. V., Xie, S. P. & Hu, S. Climate impacts of a weakened Atlantic Meridional Overturning Circulation in a warming climate. *Sci. Adv.* **6**, 1–9 (2020).
9. Timmermann, A. et al. The influence of a weakening of the Atlantic Meridional Overturning Circulation on ENSO. *J. Clim.* **20**, 4899–4919 (2007).
10. Flower, B. P., Williams, C., Hill, H. W. & Hastings, D. W. Laurentide ice sheet meltwater and the Atlantic Meridional Overturning Circulation during the last glacial cycle: a view from the Gulf of Mexico. *Abrupt Clim. Chang. Mech. Patterns, Impacts* 39–56 (2013).
11. Vetter, L., Spero, H. J., Eggins, S. M., Williams, C. & Flower, B. P. Oxygen isotope geochemistry of Laurentide ice-sheet meltwater across Termination I. *Quat. Sci. Rev.* **178**, 102–117 (2017).
12. Stommel, H. Thermohaline convection with two stable regimes of flow. *Tellus* **13**, 224–230 (1961).
13. Rahmstorf, S. Bifurcations of the Atlantic thermohaline circulation in response to changes in the hydrological cycle. *Nature* **378**, 145–149 (1995).

14. Lenton, T. M. et al. Tipping elements in the Earth's climate system. *Proc. Natl Acad. Sci. USA* **105**, 1786–1793 (2008).

15. Wood, R. A., Rodríguez, J. M., Smith, R. S., Jackson, L. C. & Hawkins, E. Observable low-order dynamical controls on thresholds of the Atlantic Meridional Overturning Circulation. *Clim. Dyn.* **53**, 6815–6834 (2019).

16. Rahmstrof, S. et al. Thermohaline circulation hysteresis: a model intercomparison. *Geophys. Res. Lett.* **32**, 1–5 (2005).

17. An, S.-I., Kim, H.-J. & Kim, S.-K. Rate-dependent hysteresis of the Atlantic Meridional Overturning Circulation system and its asymmetric loop. *Geophys. Res. Lett.* **48**, e2020GL090132 (2021).

18. Hawkins, E. et al. Bistability of the Atlantic overturning circulation in a global climate model and links to ocean freshwater transport. *Geophys. Res. Lett.* **38**, 1–6 (2011).

19. Liu, W., Xie, S.-P., Liu, Z. & Zhu, J. Overlooked possibility of a collapsed Atlantic Meridional Overturning Circulation in warming climate. *Sci. Adv.* **3**, 1–8 (2017).

20. Hu, A. et al. Role of the Bering Strait on the hysteresis of the ocean conveyor belt circulation and glacial climate stability. *Proc. Natl Acad. Sci. USA* **109**, 6417–6422 (2012).

21. Mandel, P. & Erneux, T. The slow passage through a steady bifurcation: delay and memory effects. *J. Stat. Phys.* **48**, 1059–1070 (1987).

22. Baer, S. M., Erneux, T. & Rinzel, J. The slow passage through a Hopf bifurcation: delay, memory effects, and resonance. *SIAM J. Appl. Math.* **49**, 55–71 (1989).

23. Baer, S. M. & Gaekel, E. M. Slow acceleration and deacceleration through a Hopf bifurcation: power ramps, target nucleation, and elliptic bursting. *Phys. Rev. E - Stat. Nonlinear, Soft Matter Phys.* **78**, 1–7 (2008).

24. Hughes, T. P., Linares, C., Dakos, V., van de Leemput, I. A. & van Nes, E. H. Living dangerously on borrowed time during slow, unrecognized regime shifts. *Trends Ecol. Evol.* **28**, 149–155 (2013).

25. Bergeot, B., Almeida, A., Gazengel, B., Vergez, C. & Ferrand, D. Response of an artificially blown clarinet to different blowing pressure profiles. *J. Acoust. Soc. Am.* **135**, 479–490 (2014).

26. Ritchie, P. D. L., Clarke, J. J., Cox, P. M. & Huntingford, C. Overshooting tipping point thresholds in a changing climate. *Nature* **592**, 517–523 (2021).

27. Cessi, P. A simple box model of stochastically forced thermohaline flow. *J. Phys. Oceanogr.* **24**, 1911–1920 (1994).

28. Ashwin, P., Wieczorek, S., Vitolo, R. & Cox, P. Tipping points in open systems: bifurcation, noise-induced and rate-dependent examples in the climate system. *Philos. Trans. R. Soc. A Math. Phys. Eng. Sci.* **370**, 1166–1184 (2012).

29. Dansgaard, W. et al. Evidence for general instability of past climate from a 250-kyr ice-core record. *Nature* **364**, 218–220 (1993).

30. Zahn, R. et al. Thermohaline instability in the North Atlantic during melt water events: stable isotope and ice-rafted detritus records from core SO75-26KL, Portuguese margin. *Paleoceanography* **12**, 696–710 (1997).

31. Kissel, C., Laj, C., Piotrowski, A. M., Goldstein, S. L. & Hemming, S. R. Millennial-scale propagation of Atlantic deep waters to the glacial Southern Ocean. *Paleoceanography* **23**, 1–7 (2008).

32. Deschamps, P. et al. Ice-sheet collapse and sea-level rise at the Bølling warming 14,600 years ago. *Nature* **483**, 559–564 (2012).

33. Bard, E. et al. Deglacial sea-level record from Tahiti corals and the timing of global meltwater discharge. *Nature* **382**, 241–244 (1996).

34. Menviel, L., Timmermann, A., Friedrich, T. & England, M. H. Hindcasting the continuum of Dansgaard-Oeschger variability: mechanisms, patterns and timing. *Clim* **10**, 63–77 (2014).

35. Gregoire, L. J., Payne, A. J. & Valdes, P. J. Deglacial rapid sea level rises caused by ice-sheet saddle collapses. *Nature* **487**, 219–222 (2012).

36. Fairbanks, R. G. 17,000-year glacio-eustatic sea level record: influence of glacial melting rates on the Younger Dryas event and deep-ocean circulation. *Nature* **342**, 637–642 (1989).

37. Mikolajewicz, U., Crowley, T. J., Schiller, A. & Voss, R. Modelling teleconnections between the North Atlantic and North Pacific during the younger Dryas. *Nature* **387**, 384–387 (1997).

38. Lin, Y. et al. A reconciled solution of Meltwater Pulse 1A sources using sea-level fingerprinting. *Nat. Commun.* **12**, 2015 (2021).

39. Trusel, L. D. et al. Nonlinear rise in Greenland runoff in response to post-industrial Arctic warming. *Nature* **564**, 104–108 (2018).

40. Bevis, M. et al. Accelerating changes in ice mass within Greenland, and the ice sheet's sensitivity to atmospheric forcing. *Proc. Natl Acad. Sci. USA* **116**, 1934–1939 (2019).

41. Bakker, P. et al. Fate of the Atlantic Meridional Overturning Circulation: strong decline under continued warming and Greenland melting. *Geophys. Res. Lett.* **43**, 12,252–12,260 (2016).

42. Böning, C. W., Behrens, E., Biastoch, A., Getzlaff, K. & Bamber, J. L. Emerging impact of Greenland meltwater on deepwater formation in the North Atlantic Ocean. *Nat. Geosci.* **9**, 523–527 (2016).

43. Caesar, L., Rahmstorf, S., Robinson, A., Feulner, G. & Saba, V. Observed fingerprint of a weakening Atlantic Ocean overturning circulation. *Nature* **556**, 191–196 (2018).

44. Barletta, V. R., Sørensen, L. S. & Forsberg, R. Scatter of mass changes estimates at basin scale for Greenland and Antarctica. *Cryosphere* **7**, 1411–1432 (2013).

45. Hofer, S. et al. Greater Greenland Ice Sheet contribution to global sea level rise in CMIP6. *Nat. Commun.* **11**, 1–11 (2020).

46. Kim, H.-J., An, S.-I., Kim, S.-K. & Park, J.-H. Feedback processes modulating the sensitivity of Atlantic thermohaline circulation to freshwater forcing timescales. *J. Clim.* **34**, 5081–5092 (2021).

47. Haskins, R. K., Oliver, K. I. C., Jackson, L. C., Drijfhout, S. S. & Wood, R. A. Explaining asymmetry between weakening and recovery of the AMOC in a coupled climate model. *Clim. Dyn.* **53**, 67–79 (2019).

48. Alkhayuon, H., Ashwin, P., Jackson, L. C., Quinn, C. & Wood, R. A. Basin bifurcations, oscillatory instability and rate-induced thresholds for AMOC in a global oceanic box model. *Proc. R. Soc. A* **475**, 20190051 (2019).

49. Lohmann, J. & Ditlevsen, P. D. Risk of tipping the overturning circulation due to increasing rates of ice melt. *Proc. Natl Acad. Sci. USA* **118**, 1–6 (2021).

50. Goosse, H. et al. Description of the Earth system model of intermediate complexity LOVECLIM version 1.2. *Geosci. Model Dev.* **3**, 603–633 (2010).

51. Opsteegh, J. D., Haarsma, R. J., Selten, F. M. & Kattenberg, A. ECBILT: a dynamic alternative to mixed boundary conditions in ocean models. *Tellus, Ser. A Dyn. Meteorol. Oceanogr.* **50**, 348–367 (1998).

52. Goosse, H. & Fichefet, T. Importance of ice-ocean interactions for the global ocean circulation: A model study. *J. Geophys. Res. Ocean.* **104**, 23337–23355 (1999).

53. Brovkin, V., Ganopolski, A. & Svirezhev, Y. A continuous climate-vegetation classification for use in climate-biosphere studies. *Ecol. Modell.* **101**, 251–261 (1997).

54. Blaschek, M., Bakker, P. & Renssen, H. The influence of Greenland ice sheet melting on the Atlantic Meridional Overturning Circulation during past and future warm periods: a model study. *Clim. Dyn.* **44**, 2137–2157 (2015).

AUTHOR CONTRIBUTIONS

S.-K.K. performed the research and wrote a draft of the paper. S.-K.K. designed and performed the Stommel's model experiment. H.-J.K. and S.-K.K. designed the LOVECLIM experiment, and H.-J.K. carried out the LOVECLIM run and post-data processing. S.-K.K., H.-J.K., H.A.D. and S.-I.A. analyzed and discussed the results of the paper.

COMPETING INTERESTS

The authors declare no competing interests.

ADDITIONAL INFORMATION

Supplementary information The online version contains supplementary material available at https://doi.org/10.1038/s41612-022-00236-8.

Correspondence and requests for materials should be addressed to Soon-Il An.

Reprints and permission information is available at http://www.nature.com/reprints

Publisher's note Springer Nature remains neutral with regard to jurisdictional claims in published maps and institutional affiliations.